https://doi.org/10.5194/egusphere-2026-61
Preprint. Discussion started: 15 January 2026

Aircraft-derived particle fluxes distinguish entrainment zone and decoupled layer nucleation in marine boundary layers

Ajmal Rasheeda Satheesh[1], Markus D. Petters[2], and Nicholas Meskhidze[1]

[1]Department of Marine, Earth, and Atmospheric Sciences, North Carolina State University, Raleigh, NC 27695, USA.
[2]Department of Chemical and Environmental Engineering, University of California, Riverside, CA 92521, USA.

Corresponding author: Nicholas Meskhidze (nmeskhidze@ncsu.edu)

Abstract New particle formation (NPF) in marine boundary layers plays a critical role in cloud condensation nuclei (CCN) budgets and aerosol–cloud interactions, yet the vertical distribution of NPF sources, critical for predicting CCN production efficiency, remains poorly constrained. We identified the vertical location of NPF events by deriving turbulent fluxes of 3–10 nm particles from aircraft measurements during the Aerosol and Cloud Experiments in the Eastern North Atlantic (ACE-ENA) campaign. To overcome stationarity limitations of traditional eddy covariance methods, we applied continuous wavelet transform analysis to data collected during June–July 2017 and January–February 2018 flights over the Azores. Our flux-based analysis revealed two distinct NPF scenarios with fundamentally different vertical structures and spatial extents. The first scenario featured nucleation in the entrainment zone, where free tropospheric air entrains into the boundary layer. The second scenario showed nucleation in the decoupled layer, a stratified region between the well-mixed surface layer and cloud-topped upper boundary layer. Both cases exhibited strong downward particle fluxes driven by similar mechanisms: air masses from different layers and mixing, which diluted aerosols to very low particle surface area, creating favorable nucleation conditions. NPF occurred in 15% of flights, challenging prevailing theoretical expectations that NPF should rarely occur in marine boundary layers due to high condensation and coagulation sinks from sea spray aerosols. Aircraft-derived aerosol fluxes provide essential observational constraints on the vertical distribution and source strength of new particle formation in marine environments, enabling improved representation of these processes in climate models.

1. Introduction

Cloud adjustments due to aerosols constitute one of the most significant uncertainties in climate modeling (Intergovernmental Panel on Climate Change (IPCC), 2023). The magnitude of anthropogenic aerosol radiative forcing over the industrial period is strongly influenced by the abundance and properties of natural aerosols (Andreae, 2007; Carslaw et al., 2013; Hoose et al., 2009; Meskhidze et al., 2011). While uncertainties in aerosol radiative forcing from different processes (emissions, long-range transport, new particle formation, and removal) vary spatially, marine boundary layer (MBL) cloud microphysical properties exhibit the highest sensitivity to aerosol changes (Bellouin et al., 2020; Zhang et al., 2024). Understanding how marine low level clouds and their radiative effects respond to changing aerosol load is important due to their extensive spatial coverage, low optical thickness, and low background cloud condensation nuclei (CCN) concentrations. The response of these clouds to changes in aerosol loading remains

https://doi.org/10.5194/egusphere-2026-61
Preprint. Discussion started: 15 January 2026

poorly constrained and represents a key source of uncertainty in climate projections (Zhang et al., 2024). Consequently, understanding aerosol composition, dynamics, and the mechanisms controlling CCN number budgets within the MBL is critical for improving climate models and reducing predictive uncertainties.

Previous studies have identified three primary aerosol sources in remote MBLs: (1) long-range continental transport (Logan et al., 2014), (2) downward mixing of particles formed in the free troposphere (FT) through new particle formation (NPF) mechanisms (Clarke et al., 2013), and (3) sea spray emissions (Quinn et al., 2017). NPF occurring either near the top of stratocumulus cloud decks within open-cell regions (Petters et al., 2006) or in the upper portions of mid-latitude MBLs (Zheng et al., 2021) has been suggested as an important in-situ aerosol source within the MBL. However, the difficulty in capturing actual nucleation events and determining their precise vertical location has led to the prevailing theoretical view that NPF should rarely occur in remote marine boundary layers over open oceans. This expectation is based on the relatively high surface area of sea spray aerosols, which act as condensation and coagulation sinks for nucleating vapors and newly formed particles (Bates et al., 1998; Pirjola et al., 2000).

Determining the vertical origin of freshly nucleated particles, whether from the free troposphere, the interfacial layer near the marine boundary layer–free troposphere boundary, or the interface between the well-mixed marine boundary layer and decoupled layer, has critical implications for both fundamental understanding and climate modeling. Knowledge of where nucleation occurs is essential for understanding aerosol formation mechanisms and enabling climate models to accurately simulate aerosol number size distributions required for radiative calculations. Most atmospheric models have historically assumed that nucleation should be negligible in marine boundary layers, instead predicting that particle formation would be favored at high altitudes where both temperature and aerosol surface area are substantially lower. However, traditional time-averaged aerosol concentration measurements from aircraft campaigns provide limited information about the precise vertical location where nucleation events occur. This limitation has prevented definitive identification of nucleation zones within the marine boundary layer and hampered efforts to constrain the relative importance of different aerosol sources to marine CCN budgets. Without direct observational evidence of where particles form, climate models continue to rely on theoretical assumptions that may not accurately represent actual nucleation processes in marine environments.

To address this critical knowledge gap, vertical turbulent flux measurements of freshly nucleated particles have emerged as particularly valuable tools for characterizing the vertical location of particle nucleation (Islam et al., 2022). The flux direction provides direct evidence of nucleation location: positive (upward) fluxes indicate nucleation below the aircraft, while negative (downward) fluxes suggest nucleation above the aircraft. This approach offers unprecedented spatial and temporal resolution for identifying nucleation zones that cannot be detected through conventional concentration measurements alone. In this study, we derive vertical turbulent fluxes of 3–10 nm particles using data collected during the Aerosol and Cloud Experiments in the Eastern North Atlantic (ACE-ENA) campaign. The campaign comprised two intensive operational periods (IOPs) – summer 2017 and winter 2018 – utilizing the G1 research aircraft from the DOE Atmospheric Radiation Measurement (ARM) program. By applying continuous wavelet transform techniques to high-frequency aircraft measurements, we provide the first direct observational constraints on the vertical distribution of new particle formation in remote marine boundary layers, enabling improved representation of aerosol sources in climate models.

https://doi.org/10.5194/egusphere-2026-61
Preprint. Discussion started: 15 January 2026

2. Materials and Methods

2.1 Sampling Site

The Department of Energy Atmospheric Radiation Measurement (DOE–ARM) Eastern North Atlantic (ENA) facility is positioned on Graciosa Island within the Azores archipelago, located in the northeastern Atlantic Ocean to the west of Portugal (Mather and Voyles, 2013). Air mass transport to this location follows four main pathways: (1) polluted outflow from North American sources, (2) continental emissions originating from northern European regions, (3) relatively clean Arctic air masses, and (4) air masses that recirculate within the Azores High pressure system (Wood et al., 2015; Zheng et al., 2018). The location is characterized by a low average annual aerosol optical depth (AOD) of 0.12 (Logan et al., 2014).

Data collection for this research occurred during the ACE-ENA field campaign, which included two intensive observation periods (IOPs): the initial period ran from June 21 to July 20, 2017, while the second period extended from January 15 to February 18, 2018 (Wang et al., 2019). All data from the ARM ENA site are publicly accessible through the ARM Data Discovery tool.

2.2 Instrumentation

This study utilized datasets from the ARM Aerial Facility (Schmid et al., 2014). The G–1 research aircraft was equipped with over 50 instruments for comprehensive measurements of aerosols, clouds, and atmospheric processes. Detailed information regarding flight patterns executed during the campaign can be found in (Wang et al., 2019).

Two Condensation Particle Counters (CPCs, models 3025A and 3772, TSI Inc.) with nominal 50% counting efficiency cutoff diameters of 3 nm and 10 nm, respectively, sampled through an isokinetic inlet exhibiting >90% efficiency for particles with aerodynamic diameters below 5 µm. The concentration of 3–10 nm sized particles was calculated as the difference between these CPC measurements and is denoted as $N_{3–10}$ throughout this paper. Since the measurements did not extend to particle sizes small enough to directly identify nucleation events, we follow (Islam et al., 2022) in using the term "small particle event" (SPE) to characterize these observations. The CPC 3772 operated at a constant 1 LPM flow rate maintained by an external pump and critical orifice (Fan and Pekour, 2018), while the CPC 3025A sample flow rate was not actively controlled. Both flow rates remained stable across the sampling altitude range (Zheng et al., 2021). The airborne CPC configuration was validated for operation up to 4000 m altitude and across ambient relative humidity conditions of 0–90% RH. For a typical polluted environment (~ 5000 cm^{-3}), CPC concentration measurements had an accuracy of 0.3 % (Kuang and Mei, 2019). All data used in this study passed instrument mentor specified quality control filters, which are distributed alongside the data.

Vertical wind speed (w) was measured using the Aircraft Integrated Meteorological Measurement System probe (AIIMS–20, Aventech Research Inc.). The raw measurements define downward movement as positive; therefore, the sign was inverted to align with meteorological convention (positive values indicating updrafts and negative values indicating downdrafts). Although measurements were recorded at 20 Hz, they were downsampled to 1 Hz to match the temporal resolution of the CPC data acquisition.

Aerosol size distributions from 10 nm to 600 nm were characterized using a Fast Integrated Mobility Spectrometer (FIMS) (Kulkarni and Wang, 2006a, b). The FIMS provides high temporal resolution measurements with excellent

https://doi.org/10.5194/egusphere-2026-61
Preprint. Discussion started: 15 January 2026

sensitivity and counting statistics required for aircraft-based studies (Olfert et al., 2008). Particles are charged within the instrument and separated by electrical mobility using an applied electric field. The separated particles are subsequently grown into supermicron droplets in a condenser and imaged with a high-speed camera. This approach enables the FIMS to deliver size distribution measurements comparable to those of Scanning Mobility Particle Sizers (SMPS), but at a significantly higher time resolution. This study employed an advanced FIMS configuration utilizing a spatially varying electric field that extends the measurement range from 10 nm to 600 nm (Wang et al., 2017b, a). Size distribution measurements were normalized to dry conditions; therefore, reported size distributions and number concentrations do not represent ambient humidity conditions. Cloud contamination filters were applied to prevent misclassification of cloud droplets as aerosol particles, with detailed filtering procedures described in the following section. FIMS-derived number concentration also served as a quality control flag for the 3772 CPC, where CPC concentrations less than 10% of corresponding FIMS concentrations were excluded from analysis.

A single-particle soot photometer (SP2) measured refractory black carbon concentrations in the 50 nm – 500 nm size range. While the SP2 detects individual particles and can provide number concentrations, this study reports mass concentrations (ng m^{-3}) (Schwarz et al., 2006). A high-resolution time-of-flight aerosol mass spectrometer (HR-ToF-AMS) measured bulk nonrefractory aerosol composition including sulfate, nitrate, ammonium, and organics. Dimethylsulfide (DMS) concentrations were measured using a quadruple high-sensitivity Proton-Transfer-Reaction Time-of-Flight Mass Spectrometer (PTR-ToF-MS). Due to measurement uncertainties (Zheng et al., 2021) DMS data indicate presence along the flight track rather than providing precise quantification. All data products are publicly available through the ARM DOE website with citations in the data availability section and have undergone quality control by instrument mentors. Additional technical details are available in the corresponding citations.

2.3 Data Reduction

2.3.1 Droplet shattering and cloud contamination

Droplet shattering represents a significant source of measurement contamination in airborne aerosol sampling studies. Weber et al., (1998) described this phenomenon as the fragmentation of cloud droplets during in-cloud measurements, which can produce artifacts as small as 3 nm that appear in sampling instruments. Similarly, Korolev and Isaac, (2005) documented comparable shattering effects with ice particles. While a detailed examination of the physical mechanisms behind droplet shattering lies beyond this study's scope, it is essential to filter such artifacts from our dataset to prevent misidentification of SPEs.

Cloud contamination was systematically detected and eliminated by calculating liquid water content (LWC) using the approach of Zheng et al., (2021), which utilizes droplet size spectra from the Fast Cloud Droplet Probe (FCDP). Visual data examination established a detection threshold of $3x10^{-3}$ g m^{-3}, comparable to the 10^{-3} g m^{-3} threshold employed by Zheng et al., (2021). Data exceeding this LWC threshold were excluded from analysis.

https://doi.org/10.5194/egusphere-2026-61
Preprint. Discussion started: 15 January 2026

2.3.2 Time lag correction

Accurate temporal alignment is critical for flux computations when data originate from multiple instruments in field campaigns. For tower-based or surface measurement systems, temporal synchronization typically employs cross-correlation analysis in which the vertical velocity time series is temporarily shifted (forward or backward) relative to the particle concentration time series (Stull, 1988). Although inlets are usually positioned in close proximity to sample identical air masses, this temporal adjustment is necessary to account for potential transport delays to detectors, which are often located at different positions on the tower. This approach operates on the principle that flux calculations (cross-correlation values) reach their maximum when both signals are optimally synchronized, thereby enabling accurate lag time determination. Similar analysis is essential for aircraft data processing to account for both signal delay (when inlets share the same location, but detectors are positioned differently) and spatial separation effects (when inlets themselves are located at different positions on the aircraft).

Platform-Specific Measurement Characteristics: Flux measurements differ fundamentally between tower-based and aircraft platforms in their spatial and temporal sampling characteristics. Tower measurements provide continuous observations at fixed heights, capturing the complete turbulent eddy spectrum within the atmospheric boundary layer, including low-frequency contributions essential for accurate flux estimates (Helbig et al., 2021; Sakai et al., 2001). Aircraft measurements sample different air masses as the platform moves horizontally, effectively trading temporal for spatial averaging (Desjardins et al., 1989). Aircraft measurements at higher boundary layer altitudes face additional challenges. In convective boundary layers, turbulent intensity increases with height above the surface layer before decreasing after 0.3–0.4 z_i (where z_i is the boundary layer height), requiring measurement lengths of 100 to 10^4 times the boundary layer height to maintain flux variance within 10% (Lenschow and Stankov, 1986). For aircraft traveling at 100 m s^{-1}, a 10 Hz sampling system resolves eddies as small as 20 m, while a 1 Hz sampling system resolves eddies down to 200 m.

Tower measurements easily satisfy stationarity requirements through 30-minute averaging periods, whereas aircraft measure turbulence over large areas much faster but must assume spatial homogeneity along the flight path (Gioli et al., 2004). High aircraft speeds introduce additional constraints on sensor response times and spatial resolution, as instruments must respond quickly enough to resolve the smallest relevant eddies, a challenge that intensifies at higher flight speeds and lower altitudes where smaller eddy sizes result in higher observed frequencies when sampled by fast-moving aircraft (Desjardins et al., 1989)

CPC synchronization validation: Since the CPCs used in this study were connected to the same isokinetic inlet from different positions, confirmation was needed that they sampled identical air masses simultaneously. Supplementary Figure S1 shows particle concentration measurements from both CPCs for a representative day. Although the absolute values differ as expected due to their different size detection limits (3 nm vs. 10 nm), the temporal patterns closely align. In Supplementary Figure S2, the Spearman correlation coefficient (ρ) was calculated for the particle concentration measured from both CPCs after removing cloud shattering artifacts and excluding data corresponding to small particle events (SPEs), since only the ultrafine CPC can detect SPEs (selection criteria will be discussed in subsequent sections). From the complete campaign dataset, 370 seconds of data were randomly selected to avoid selection biases, yielding an average ρ of 0.97. The entire CPC dataset was segmented into 20-second intervals

https://doi.org/10.5194/egusphere-2026-61
Preprint. Discussion started: 15 January 2026

(representing the time taken for the airplane to traverse 2 km), and lag times were determined using covariance maximization. Supplementary Figure S3 shows the analysis results, suggesting that lag times of 0 and 1 seconds occurred in 13% and 27% of cases, respectively. Since no single lag time was sufficiently prevalent to apply uniformly across the entire campaign, individual lag times were determined prior to each flux calculation.

Pressure-based lag time determination: As the vertical wind speed and the CPC measurements were taken from different parts of the aircraft, determining the time lag was essential to ensure that both the AIMMS–20 probe and the isokinetic inlet sampled air masses from identical locations. To achieve this, the pressure measured at the isokinetic inlet was compared with the static pressure measured by the Rosemount 1201F1 pressure sensor mounted on the AIMMS–20 probe. Supplementary Figure S4 shows the time series of measured pressure from both inlets for a representative day, demonstrating that both measurements follow similar pressure variation patterns at 1 Hz temporal resolution.

Supplementary Figure S5 shows the Spearman correlation coefficient for the pressure measurements from both inlets. Data selection followed the same approach used for CPC data, though without filtering for cloud shattering or SPEs since these phenomena do not affect pressure measurements. The correlation coefficient was 0.99, suggesting negligible lag between the instruments. We applied the same covariance maximization technique used for the CPC data analysis. As shown in Figure S6, no single lag time was appropriate for the entire campaign. Consequently, individual lag times were calculated for each case.

2.4 Aerosol number flux calculations

As previously discussed, maintaining stationarity conditions presents significant challenges for aircraft-based measurements due to the platform's high velocity, which fundamentally alters the sampling framework compared to stationary tower measurements (Islam et al., 2022). To address this limitation, this study employs the continuous wavelet transform (CWT) method for flux derivation. The primary advantage of the CWT approach over traditional methods is that it does not require stationarity conditions and eliminates the need for data detrending, thereby preventing systematic errors that can arise from linear detrending procedures in flux calculations (Rannik and Vesala, 1999). This study follows the method developed by (Torrence and Compo, 1998) for CWT flux derivation. The wavelet coefficient, $W_N(a,b)$, for a function $x(z)$ which changes with height, is calculated as a function of both location (height for airborne measurements or time for ground-based measurements) and scale (frequency or wavenumber) through convolution with a wavelet function (ψ):

$$W_N(a,b) = \int_{-\infty}^{\infty} x(z)\,\psi_{a,b}(z)dz \quad (1)$$

where $\psi_{a,b}(z)$ represents the wavelet function, controlled by the scale parameter (a) and translation parameter (b). The scale parameter governs the wavelet frequency, while the translation parameter shifts it in the temporal domain. The wavelet function is defined as:

$$\psi_{a,b}(z) = \frac{1}{\sqrt{a}}\psi_0\left(\frac{z-b}{a}\right) \quad (2)$$

https://doi.org/10.5194/egusphere-2026-61
Preprint. Discussion started: 15 January 2026

All wavelet functions are based on a "mother" wavelet, ψ_0. For this study, the Morlet wavelet is chosen as the mother wavelet, which is the product of a plane wave with a Gaussian function (Torrence and Compo, 1998). Schaller et al., (2017) reported that the Morlet wavelet provides reliable results in flux analysis even when traditional eddy covariance methods fail.

$$\psi_0(\eta) = \pi^{\frac{-1}{4}} e^{i\omega_0\eta} e^{\frac{-\eta^2}{2}} \quad (3)$$

where ω_0 is the non–dimensional frequency (set to 6 for this study) and η is the non–dimensional time parameter and $\eta = \frac{z-b}{a}$, the first exponential term is the complex sinusoid, and the second exponential term is the Gaussian envelope. Using this methodology, the vertical turbulent particle flux can be calculated according to (Schaller et al., 2017; Torrence and Compo, 1998) as:

$$\overline{w'(z)N'_{3-10}(z)} = \frac{\delta_t}{C_\delta} \times \frac{\delta_j}{L} \times \sum_{n=0}^{L-1} \sum_{j=0}^{J} \left[\frac{W_N(a,b) \times W_W^*(a,b)}{a(j)} \right] \quad (4)$$

C_δ, the wavelet specific reconstruction factor is taken as 0.776, which is empirically derived for the chosen wavelet (Schaller et al., 2017; Torrence and Compo, 1998) , L represents the number of elements in the time series with timestep δ_t which is the inverse of frequency (1 Hz for this study), J is the maximum number of scales with δ_j being the space between each discrete scale (Schaller et al., 2017; Torrence and Compo, 1998).

$$J = \delta_j^{-1} \times log_2\left(\frac{L \times \delta_t}{s_0}\right) \quad (5)$$

δ_j was chosen to be 0.25 s (Schaller et al., 2017; Torrence and Compo, 1998), this value can be adjusted to get better scale resolution at the expense of higher computational cost, s_0 is the smallest scale of the wavelet taken as $2\delta_t$, *a(j)* is the scale parameter for the discrete scale calculated as:

$$a(j) = s_0 \times 2^{j\delta j} \qquad j = 0,1,.....J \quad (6)$$

$W_N(a,b)$ is the wavelet coefficient for the particle concentration signal, and $W_w^*(a,b)$ is the complex conjugate of the wavelet coefficient for the vertical velocity signal. Under stationary conditions, fluxes calculated using both CWT and traditional eddy covariance methods should yield equivalent results, though agreement may vary in aircraft measurements due to the presence of non-stationarities (Misztal et al., 2014; Wolfe et al., 2018).

2.5 Limit of Detection Determination

Spirig et al., (2005) demonstrated that calculating covariance at time ranges significantly larger than the integral time scale can quantify the precision of individual flux determinations. Since the integral time scale cannot be accurately determined in this study, we employ a large time range approach. The limit of detection (LoD) is defined as 1.96 times (95% confidence interval) the standard deviation of covariance between w and $N_{3\text{-}10}$ when one of the signals is

https://doi.org/10.5194/egusphere-2026-61
Preprint. Discussion started: 15 January 2026

temporarily shifted with respect to the other. Signal shifts −10 to +10 seconds (corresponding to ±1 km spatial displacement) are applied to ensure complete decoupling between the signals. Flux calculations are restricted to periods when the aircraft maintained horizontal, straight line flight segments to ensure reliable flux estimates and minimize the influence of aircraft maneuvers on turbulence measurements. The limit of detection is used as an absolute value and hence if a particular flux event is lower in absolute value compared to the LoD, they will not be considered for analysis.

2.6 Small particle events selection criteria

Establishing appropriate threshold values for new particle formation over tropical oceanic regions presents significant challenges due to sparse observational datasets and the intricate interactions between meteorological and chemical processes in these environments. Earlier studies have typically used concentration thresholds of 10^3 to 10^4 particles cm^{-3} for ultrafine particles (3–25 nm) to distinguish nucleation events from background conditions. However, these criteria were primarily established based on observations from continental or mid-latitude marine environments (Dal Maso et al., 2005; Kulmala et al., 2012). Given that tropical marine regions are characterized by reduced background aerosol loadings and distinct precursor gas profiles relative to higher latitude zones, more conservative thresholds (500–1000 particles cm^{-3}) may prove better suited for detecting nucleation phenomena in these relatively unpolluted environments (Modini et al., 2009; Weber et al., 1997). Additionally, the aircraft-based measurement method prevented the implementation of traditional nucleation event identification criteria, specifically the requirement for persistent concentration increases spanning 1–2 hours to distinguish genuine nucleation from brief local source influences (Kulmala et al., 2012).

For this study, we modified the methodology established by Zheng et al., (2021) to detect small particle events (SPEs). Individual 1-second measurements were used to identify when $N_{3–10}$ concentrations exceeded 150 cm^{-3}, once identified the measurements that exceeded the threshold were grouped into 10-second intervals (equivalent to ~1 km spatial resolution), and the average $N_{3–10}$ for the group was checked to see if it achieved statistical significance using:

$$N_3 - N_{10} > 3\sigma_D \quad (7)$$

where σ_D represents the uncertainty in the concentration difference between N_3 and N_{10}, expressed as:

$$\sigma_D = \sigma(N_3 - N_{10}) \quad (8)$$

https://doi.org/10.5194/egusphere-2026-61
Preprint. Discussion started: 15 January 2026

2.7 Frequency response and flux averaging time

Momentum, enthalpy, and matter are transported in the atmosphere by eddies of different spatial scales. One-dimensional power spectral analysis is used to decompose the signal into components of different frequencies, which are associated with different eddy sizes. Fast Fourier Transform (FFT) and Continuous Wavelet Transform (CWT) were used to calculate the power spectral density (PSD) of vertical wind speed and particle concentration.

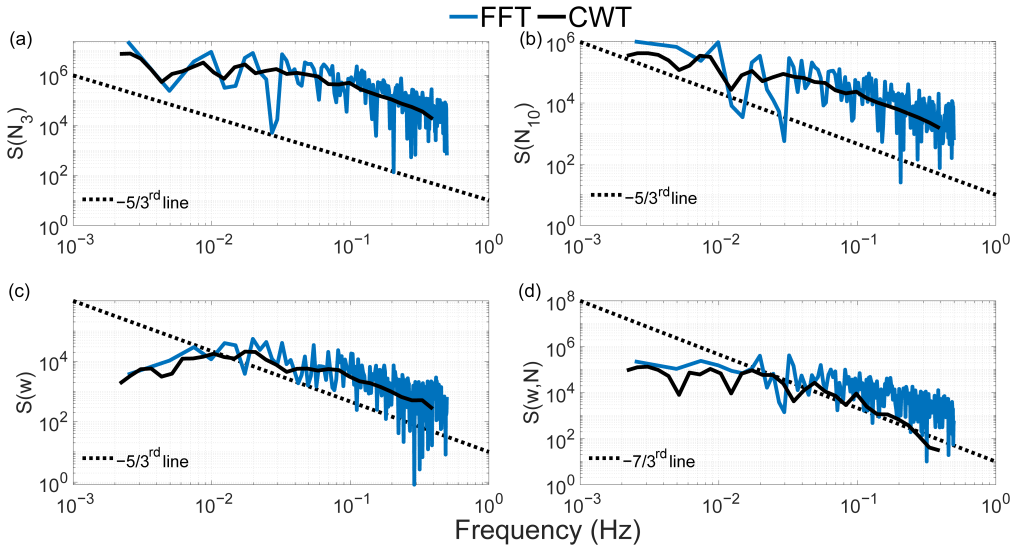

Figure 1. Power spectral density for (a) N_3, (b) N_{10}, (c) vertical wind velocity, and (d) 3-10 nm particle flux.

Figure 1 shows the PSD for a flight leg on 21 June 2017 between 13:43 and 13:49 UTC at a height of 550 m above mean sea level. Dashed lines represent the theoretical slopes for the inertial subrange, which describe how energy cascades from larger to smaller eddies and finally dissipates as heat due to viscous friction (Pope, 2000). Both particle concentration spectra (e.g., Fig. 1b) and flux spectra (Fig. 1d) exhibit deviations from the theoretical −5/3 and −7/3 Kolmogorov scaling at frequencies larger than 0.3 Hz. The spectral flattening observed at these frequencies is characteristic of white noise, suggesting instrumental limitations where the CPC cannot adequately resolve concentration fluctuations faster than ~3 sec.

Figure 1 shows some differences between FFT and CWT flux calculations, especially for fluxes at high frequencies. These differences likely stem from several key methodological differences. Aircraft data are inherently non-stationary as the platform moves through different air masses, meteorological conditions, and altitudes. FFT assumes stationarity over the entire analysis window, which can introduce artifacts at high frequencies when applied to non-stationary aircraft data. CWT can handle non-stationary signals by providing time-localized frequency information, making it more robust for aircraft measurements (Schaller et al., 2017). Li et al., (2023) evaluated uncertainties of turbulent flux calculation using eddy covariance and wavelet analysis methods, finding that "EC and Morlet-wavelet generate biases

https://doi.org/10.5194/egusphere-2026-61
Preprint. Discussion started: 15 January 2026

ranging 50–100% of the 'true' values. FFT can suffer from spectral leakage, especially at high frequencies, when the raw signal doesn't fit perfectly into the sine or cosine signal in the analysis window. This is particularly problematic for aircraft data, where turbulent structures may not be periodic over the sampling interval (Harris, 1978). CWT uses wavelets that are naturally windowed and localized, reducing leakage effects. At high frequencies corresponding to small spatial scales, aircraft measurements become increasingly challenging due to sensor response time limitations, spatial averaging effects, and platform motion artifacts (more on this in Sect. 2.8). The CWT's more conservative high-frequency response may better represent the actual resolvable flux contributions (Misztal et al., 2014).

To assess whether the calculated fluxes adequately represent both low- and high-frequency turbulent contributions, we conducted ogive analysis using the approach described by Foken et al., (2006). Mobile measurement platforms necessitate modified considerations for flux averaging intervals. Standard 30-minute averaging periods used in stationary tower observations are inappropriate for aircraft measurements. Considering the aircraft's ground speed, a 90-second sampling period covers an equivalent air mass to that sampled by a stationary sensor over 30 minutes at typical wind speeds of 5 m s^{-1}. To enable direct comparison between ogives computed using FFT and CWT methods, normalization was applied according to Sun et al., (2018):

$$\widehat{Og}(f) = \frac{Og(f)}{sgn\{max(Og(f))+min(Og(f))\}max(|Og(k)|)} \quad (9)$$

where $sgn\{x\}$ represents the signum function, returning +1 for positive x, −1 for negative x, and zero when x equals zero. When the normalized ogive equals 1, the ogive value corresponds precisely to the covariance value for that averaging period. The advantage of this normalization approach is that it facilitates the identification of cases where low-frequency turbulence has an opposite sign to high-frequency turbulence. In such situations, large and small eddies transport material in opposing directions, indicating complex atmospheric processes such as counter-gradient transport. The normalized ogive plot visually reveals these opposing contributions through characteristic rise-and-fall patterns that might otherwise be obscured in non-normalized data.

Figure 2 illustrates the ogive as a function of distance covered by the aircraft for the same flight leg shown in Fig. 1. Signal frequency was converted to distance by dividing the aircraft speed (assumed to be constant at 100 m s^{-1}) by the frequency obtained from the FFT or CWT analysis. This plot reveals that the particle flux for this flight leg can be resolved by averaging over 40 km. While both FFT and CWT ogives show agreement for this case, such consistency cannot be expected universally; therefore, CWT fluxes are used throughout this study for the reasons discussed in previous sections.

https://doi.org/10.5194/egusphere-2026-61
Preprint. Discussion started: 15 January 2026

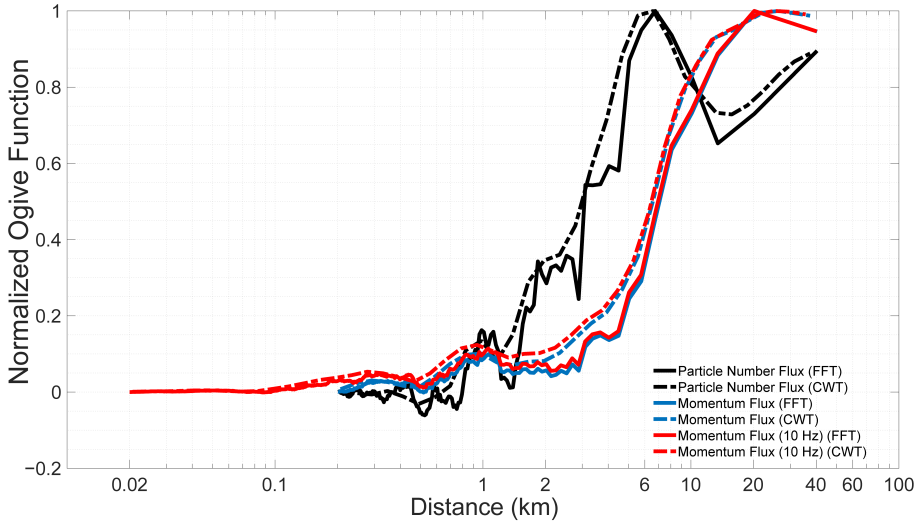

Figure 2: Normalized ogive function.

2.8 Flux loss correction

If the sensor used to measure fluxes are too slow to accurately capture the smaller eddies that contribute to the total flux, the turbulent fluxes will require correction. For micrometeorological flux measurements on towers at 10 m above the surface, instruments are typically operated at 10 Hz (Nyquist frequency = 5 Hz). Under typical wind speeds of 5 m s^{-1}, this sampling rate can resolve eddies as small as ~1 m, ensuring that most energy-containing and inertial subrange eddies are captured (Aubinet et al., 2012; Lee et al., 2005; Stull, 1988).

However, airborne flux measurements present different challenges. The integral length scales of turbulent eddies increase approximately linearly with height within the surface layer (roughly the bottom 10% of the boundary layer), then remain approximately constant above this level, limited by the boundary layer height (Kaimal and Finnigan, 1994). In the mixed layer portion of a typical boundary layer (above ~100 m surface layer), integral length scales are typically 100-200 m (Lenschow and Stankov, 1986). At an aircraft ground speed of 100 m s^{-1}, the 1 Hz sampling provides 200 m spatial resolution, which approaches but does not fully resolve the integral length scale. Consequently, the sampling resolution approaches the lower limit for adequately resolving the dominant flux-carrying scales and may under sample contributions from smaller turbulent structures.

To address this limitation, we applied the approximations from Horst (1997) to estimate the ratio of measured flux (F_m) to "true" flux (F) for different atmospheric stability conditions encountered during campaign flights:

$$\frac{F_m}{F} = \frac{1}{1+\left(2\pi n_m \tau_c \frac{\bar{u}}{z}\right)^{\alpha}} \quad (10)$$

where F_m is the measured flux, F is the "true" flux, $\bar{u}$ is the magnitude of average wind speed, z is the height of the airplane, τ_c is the response time constant of the CPC, which was taken as 3.0 s, α = 0.88, and n_m = 0.085 for neutral

https://doi.org/10.5194/egusphere-2026-61
Preprint. Discussion started: 15 January 2026

and unstable conditions (Pryor et al., 2007). Equation 10 was originally developed by Horst (1997) to estimate the attenuation of scalar flux measurements within the surface layer, but has been applied to aircraft measurements (Gioli et al., 2004), with corrected airborne fluxes showing good agreement with tower data when aircraft measurements were conducted over homogeneous surfaces at altitudes comparable to tower height.

3.0 Results

We examine two flight days as case studies of SPEs observed at varying altitudes above the ocean. Additional supporting flights are presented in the Supplementary Information for each case.

Table 1. Summary of N_{3-10} particle vertical turbulent flux estimates from aircraft campaigns with detection limits and flux loss assessment.

No	Date	Time (UTC)	Height (m)	N_{3-10} flux (cm^{-2} s^{-1})	LoD (cm^{-2} s^{-1})	F_m/F	σ^2 w_*^{-2}
Entrainment zone nucleation							
1	01/29/18	10:54:59-10:58:13	1,205	−41,092	34,423	0.97	0.01
		12:18:47-12:21:50	1,218	−2,975	2,085	0.98	0.005
2	02/10/18	13:53:20-13:55:02	1,375	−1,195	381	0.93	0.003
Decoupled layer nucleation							
3	06/21/17	14:03:30-14:09:25	800	1,139	294	0.99	0.016
		13:56:10-14:02:25	800	2,929	1,239	0.98	0.021
		13:42:40-13:49:23	550	−2,782	1,995	0.95	0.1
		13:32:20-13:38:40	30	−860	400	0.76	0.17
4	07/07/17	13:42:18-13:43:04	565	−94,093	49,410	0.86	0.02
		13:43:07-13:44:58	535	−21,317	4,959	0.90	0.031
5	02/18/18	14:17:32-14:19:38	555	298	115	0.81	0.016

https://doi.org/10.5194/egusphere-2026-61
Preprint. Discussion started: 15 January 2026

		14:47:10-14:51:34	250	−3,217	1,153	0.70	0.056
6	02/12/18	14:54:27-14:58:37	837	5,433	1,173	0.93	0.04

Case 1: SPE occurring in the entrainment zone near the top of the marine boundary layer

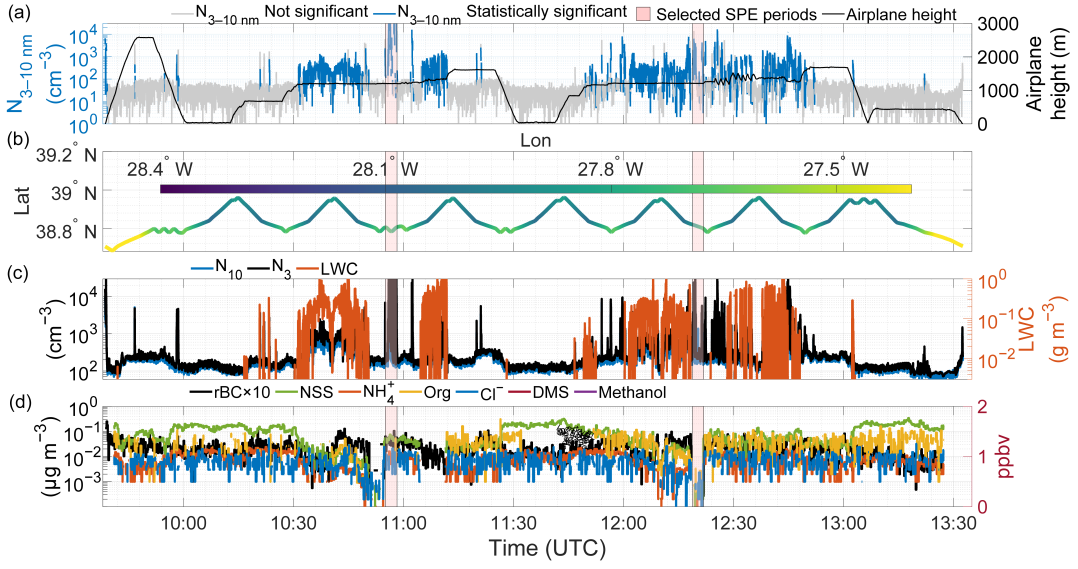

Figure 3. Multi-parameter time series during the January 29, 2018 flight showing: (a) $N_{3\text{-}10}$ particle concentrations with aircraft altitude (b) aircraft position with latitude and longitude; (c) particle number concentrations for N_{10}, N_3, and liquid water content; and (d) non-refractory aerosol chemical composition including non-seasalt sulfate (NSS), ammonium (NH_4^+), organics (Org), chlorine ion (Cl^-), refractory black carbon (rBC, multiplied by 10 for visualization) in µg m^{-3}, and trace gases dimethylsulfide (DMS) and methanol in ppbv.

Figures 3–5 present data collected on January 29, 2018 (with an additional example from February 10, 2018, shown in Supplementary Figs. S7–S9). Figure 3 presents a multi-panel time series spanning approximately 3.5 hours of flight operations. The aircraft first ascended to ~2,500 m but generally operated below ~1,500 m throughout the flight (Fig. 3a). The flight trajectory (Fig. 3b) demonstrates predominantly east-west movement across the Azores region, spanning latitudes from approximately 39.0° to 39.5°N and longitudes from −28.4° to −27.4°W. High liquid water content regions (orange in Fig. 3c) indicate frequent cloud encounters. Following our quality control procedures, all $N_{3–10}$ concentration data with liquid water presence were excluded from analysis to prevent contamination from cloud droplet shattering artifacts. The pink-shaded periods mark the intervals chosen for detailed analysis, which exhibited simultaneous increases in both N_3 and N_{10} concentrations exceeding 10^4 cm^{-3} (indicating an SPE). Figure 3d demonstrates that these periods contained no measurable liquid water and were distinguished by substantial

https://doi.org/10.5194/egusphere-2026-61
Preprint. Discussion started: 15 January 2026

concentrations (~0.1 μg m^{-3}) of non-seasalt sulfate. Organic concentrations were also elevated throughout the flight, especially during the second half.

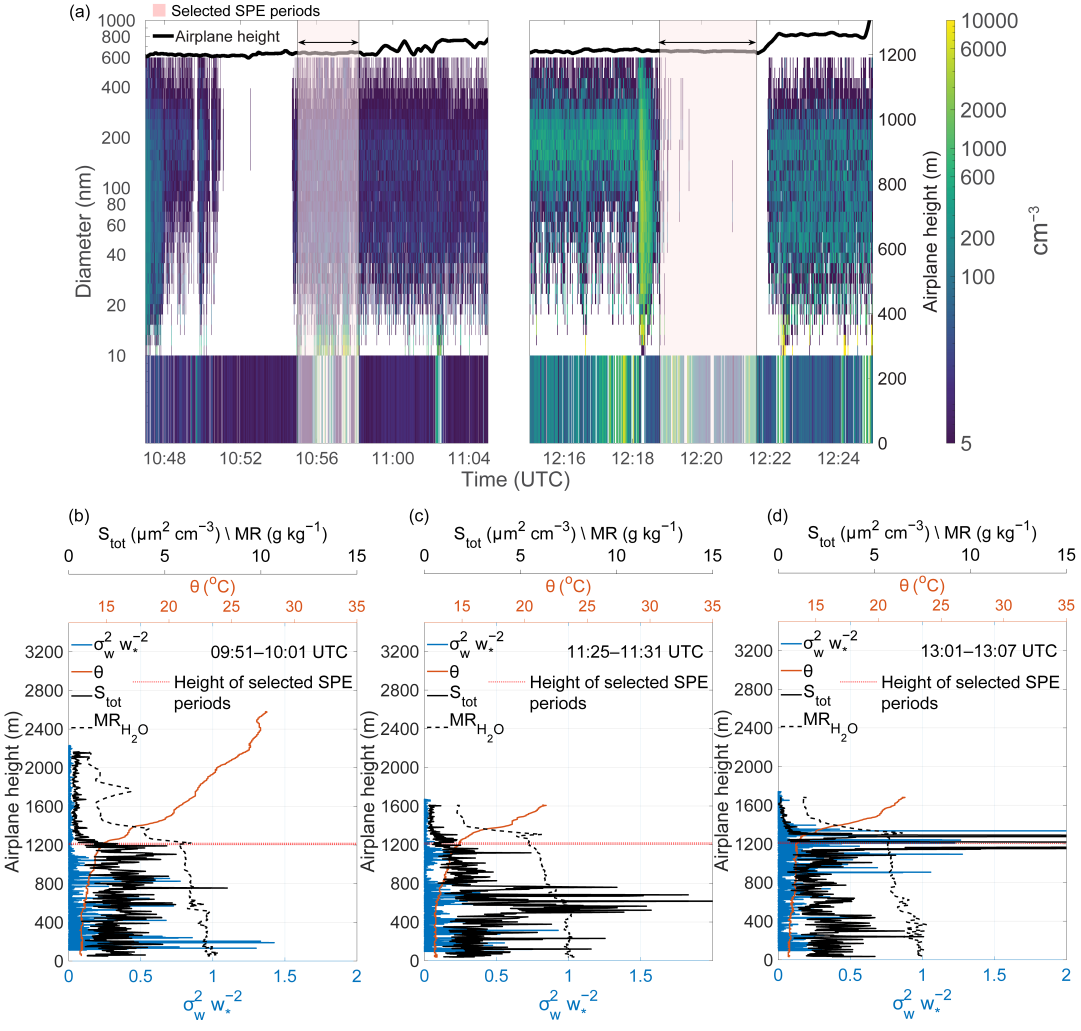

Figure 4. (a) The main panel shows size-resolved particle number concentrations (10-600 nm) from FIMS as a function of time and altitude, while $N_{3\text{-}10}$ concentrations in the lower strip. (b-d) Vertical profiles of potential temperature (θ), normalized vertical velocity variance ($\sigma_w^2\, w_*^{-2}$), particle total surface area (Stot), and water vapor mixing ratio (MR). Gaps in the time series indicate the missing data.

Figure 4a shows the temporal evolution of particle concentration between ~10:47–11:05 and ~12:15–12:25 UTC. The colormap represents FIMS-derived, size-resolved aerosol number concentrations (10–600 nm diameter), varying across time and altitude, while the lower panel displays $N_{3–10}$ concentrations. The two pink-highlighted intervals are the same as in Fig. 3. The high particle concentration ~ 12:18 UTC is likely an artifact due to cloud droplet shattering. Figures 4b–d present vertical profiles of potential temperature, normalized vertical velocity variance ($\sigma_w^2\, w_*^{-2}$) i.e., the vertical velocity variance normalized by the square of the convective velocity scale), total particle surface area,

https://doi.org/10.5194/egusphere-2026-61
Preprint. Discussion started: 15 January 2026

and the water vapor mixing ratio at three locations nearest to the pink-highlighted intervals. Sharp gradients in the potential temperature (orange) profile, often called potential temperature inversion or capping inversion, mark the top of the MBL. These gradients indicate the presence of an entrainment zone (e.g., (Boers and Eloranta, 1986)), a layer at the top of the boundary layer where free tropospheric air masses are entrained into the capping inversion and interact with convective thermals rising from below. Figures 4b–d reveal a deep boundary layer with the entrainment zone between approximately 1,200–1,400 m, consistent with previous estimates that entrainment zones typically comprise 20–40% of boundary layer depth (Martin et al., 2014).

Figures 4b–d present the profiles of ($\sigma_w^2\ w_*^{-2}$) profiles, a metric that characterizes the intensity of turbulent structures in convective boundary layers (Deardorff, 1974; Dewani et al., 2023). These profiles show elevated ($\sigma_w^2\ w_*^{-2}$) values near the ocean surface and within the entrainment zone, with minimal values in the free troposphere, where significant turbulence is absent. The sharp gradients in mixing ratios shown in Figs. 4b–d indicate moisture convergence that either precedes cloud formation or reflects recently dissipated clouds that have left behind residual moisture signatures due to changing atmospheric conditions. Figure 3 demonstrates frequent cloud encounters during this flight. Despite some vertical variability shown in Figs. 4b–d, the total particle surface area (S_{tot}) remained relatively low throughout the flight, falling well below the campaign averages of ~ 30 $\mu m^2\ cm^{-3}$ in the surface mixed layer and ~10 $\mu m^2\ cm^{-3}$ in the upper decoupled layer reported by Zheng et al. (2021). Figure 4c also shows a distinct S_{tot} maximum at an altitude where small gradients in both potential temperature and mixing ratio suggest the presence of an entrainment layer. The pronounced S_{tot} increase could indicate a nucleation occurring at this location (see Case 2 below), although this hypothesis could not be independently verified looking at the $N_{3–10}$ data in this case. Figure 4c shows that the entrainment zone and free troposphere were characterized with extremely low S_{tot} values.

Figure 5 presents the spatial distribution of $N_{3\text{-}10}$ particle concentrations along the flight path at ~1,200 m altitude (dashed lines in Figs. 4b–d). Concentrations up to 10,000 cm^{-3} indicate potential nucleation within this air mass. Previous studies identify the mixed layer or entrainment zone as the likely location for nucleation events (Größ et al., 2018; Meskhidze et al., 2019; Nilsson et al., 2001). Several mechanisms that could initiate nucleation include adiabatic cooling in the rising convective plumes, turbulent fluctuation in temperature and vapor concentration caused by entrainment flux, and dilution of mixed-layer air by the entrained air, causing a sudden decrease in preexisting aerosol concentration (Nilsson et al., 2001). Combined with extremely low preexisting particle concentrations, these processes create favorable conditions for new particle formation.

https://doi.org/10.5194/egusphere-2026-61
Preprint. Discussion started: 15 January 2026

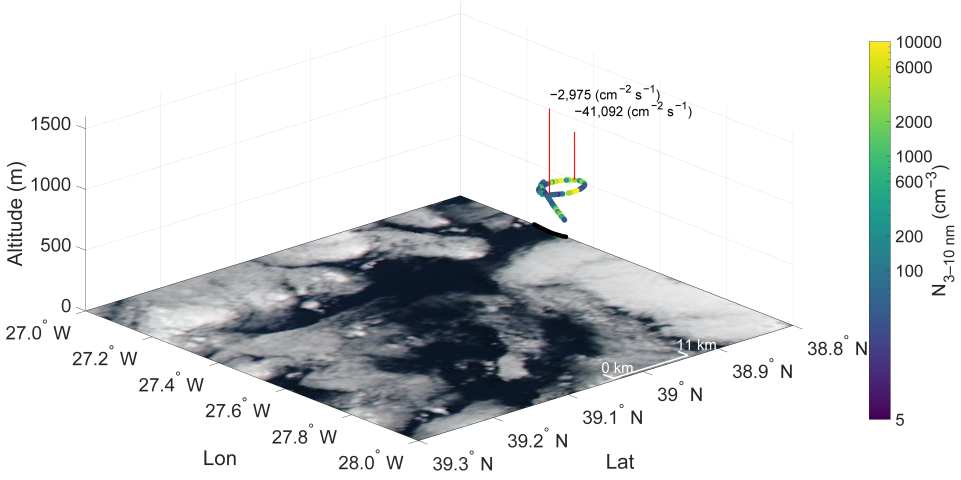

Figure 5. Spatial distribution of N_{3-10} particle concentrations along the flight track during the period highlighted in Figures 3 and 4. Mean calculated fluxes are labeled on the track. Color scale indicates particle number concentrations (cm^{-3}). The background shows a satellite-corrected reflectance image taken from the overpass at 15:15 UTC, with the ocean surface appearing dark and clouds appearing white, Credit: NASA Worldview Snapshots.

The exact spatial location and the horizontal extent of the SPE cannot be definitely determined from aircraft measurements alone. However, substantial downward flux of $N_{3–10}$ particles (−41,092 and −2,975 cm^{-2} s^{-1}) at ~1,200 m strongly suggests nucleation occurring within the entrainment zone. This interpretation is supported by the absence of $N_{3–10}$ at ~1,600 m during 11:14–11:25 and 12:51–13:01 UTC (Fig. 3). The small particle size (3–10 nm) and less than 10 km horizontal extent argue against free tropospheric nucleation, as particles would have grown and the plume would have diluted during descent. Supplementary Figs. S8 and S9 show a downward flux of $N_{3–10}$ particles (−1,195 cm^{-2} s^{-1}) at 1,375 m with complete absence of $N_{3–10}$ above ~1,400 meters, indicating SPE occurrence specifically within the entrainment zone between 1,375–1,400 m.

Figure 5 indicates the SPE horizontal extents of ~2 to 10 km. Nilsson et al., (2001) proposed that convective roll vortices, quasi-two-dimensional coherent structures manifesting as alternating updraft/downdraft bands (Etling and Brown, 1993) could enhance nucleation in the entrainment zone. These organized eddies, often related to a cold air outbreak, span the full boundary layer depth and with characteristic aspect ratios (wavelength/boundary layer depth) of 2–6 (Etling and Brown, 1993; Hartmann et al., 1997).

Figures 3–5 and the flux analysis (Table 1) demonstrate that the entrainment zone nucleation near the MBL top occurred on two days (January 29 and February 10, 2018), representing nearly 5% of flight days. Despite a relatively small horizontal extent (<10 km), these newly formed particles can be entrained in the boundary layer via vertical turbulent processes, potentially playing an important role in controlling CCN concentrations for marine clouds.

https://doi.org/10.5194/egusphere-2026-61
Preprint. Discussion started: 15 January 2026

Case 2: SPE occurring at the interface between the well-mixed surface layer and the decoupled layer

Figures 6–8 present data from June 21, 2017 (with additional examples from July 7, 2017, February 18, 2018 and February 12, 2018 shown in Supplementary Figs. S10–S12, S13–15, and S16–S18). Figure 6 shows approximately 4 hours of flight operations, with the aircraft initially operating at very low altitudes (~30 and 50 m) around 12:00 and 13:30 UTC, then gradually ascending to ~1,000 m. Multiple events with $N_{3–10}$ concentrations from 10^2 to 10^4 cm^{-3} were observed throughout the second half of the day. The flight trajectory in Fig. 6b demonstrates predominantly east-west movement, spanning latitudes from approximately 39.0° to 39.5°N and longitudes from −28.4° to −27.4°W. The pink-highlighted intervals show concurrent increases in N_3 and N_{10} concentrations exceeding 10^3 cm^{-3}, indicative of SPEs. High concentrations of both nss-sulfate and methanol persisted throughout when the aircraft remained below ~1,000 m (Fig. 6d), with methanol concentration increasing as the aircraft ascended above ~1,000 m.

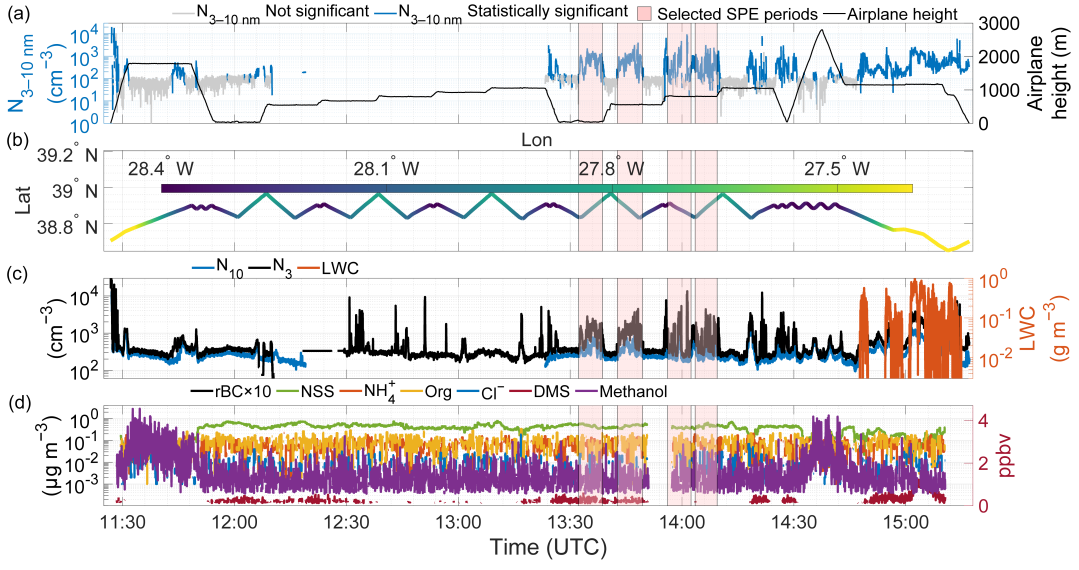

Figure 6. Same as Figure 3 but for June 21, 2017.

Figure 7a shows size-resolved particle number concentrations evolution during 13:30–14:20 UTC, encompassing the four pink-highlighted intervals from Fig. 6. The panel Fig. 7a displays $N_{3–10}$ particle concentrations. High $N_{3–10}$ concentrations were encountered at multiple altitudes, with maximum values exceeding 1,800 cm^{-3} at ~800 m.

The potential temperature and water vapor profiles (Figs. 7b,c) show the MBL structure consisting of a well mixed surface layer extending to ~ 700 m and a decoupled upper boundary layer between ~ 700–1300 m. Decoupled structures typically form from radiative heating of the cloud layer and evaporative cooling in the sub-cloud layer, which stabilize the boundary layer and suppress vertical mixing (Galewsky et al., 2022; Jones et al., 2011; Wood and Bretherton, 2004). Sharp gradients in both potential temperature and mixing ratio around 1,300 m marking the entrainment zone, above which the free troposphere begins above 1,400 m. The ($\sigma_w^2\, w_*^{-2}$) profiles show higher magnitudes in the mixed layer (indicating active turbulence) and low magnitudes in both the decoupled layer (due to

https://doi.org/10.5194/egusphere-2026-61
Preprint. Discussion started: 15 January 2026

stratification and suppressed vertical mixing) and free troposphere. Total particle surface area remained low in the mixed layer but increased considerably toward the top of the mixed layer before decreasing in the decoupled layer and reaching very low values in the free troposphere.

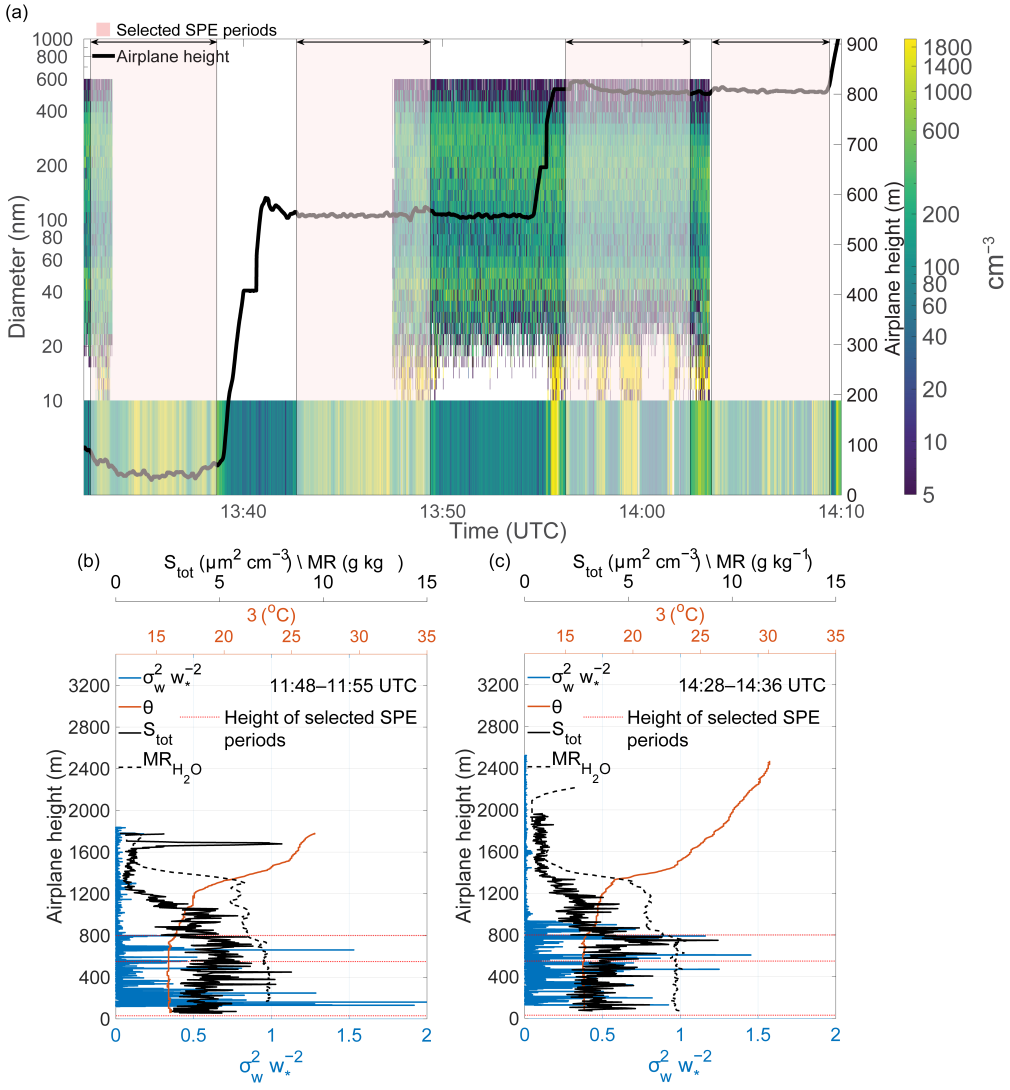

Figure 7. Same as Figure 4, but for June 21, 2017.

Figure 8 shows $N_{3–10}$ particle concentrations along flight paths at varying altitudes: 30 m, 550 m, and two segments at 800 m. We separated the 800 m path to prevent the airplane sampling the same airmass because from 13:55–14:03 UTC the aircraft flew along the prevailing wind direction, then changed direction by 90° to fly perpendicular to the

https://doi.org/10.5194/egusphere-2026-61
Preprint. Discussion started: 15 January 2026

wind. The positive vertical turbulent fluxes at 800 and negative values below suggest the SPE occurred between 550–800 meters, likely at the top of the well mixed layer or the bottom of the decoupled layer.

The nucleation processes in the entrainment zone and at the base of the decoupled layer could be mechanistically similar. Both locations feature the convergence of distinct air masses, in this case, the well-mixed surface layer and the stratified decoupled layer above, which generates turbulent mixing and aerosol dilution effects. While less pronounced than at the boundary layer top, the interface between these layers exhibits comparable thermodynamic conditions: potential temperature gradients, contrasting vapor concentrations, and localized adiabatic cooling. Figure 7 demonstrates that the decoupled layer maintains significantly lower aerosol surface area concentrations relative to the well-mixed layer below, establishing conducive conditions for nucleation when air mass mixing occurs. A key distinction, however, lies in the spatial characteristics, whereas entrainment zone nucleation showed limited horizontal extent (<10 km), the decoupled layer event spanned at least 50–60 km, suggesting either more persistent favorable conditions or a fundamentally different source mechanism operating over regional scales.

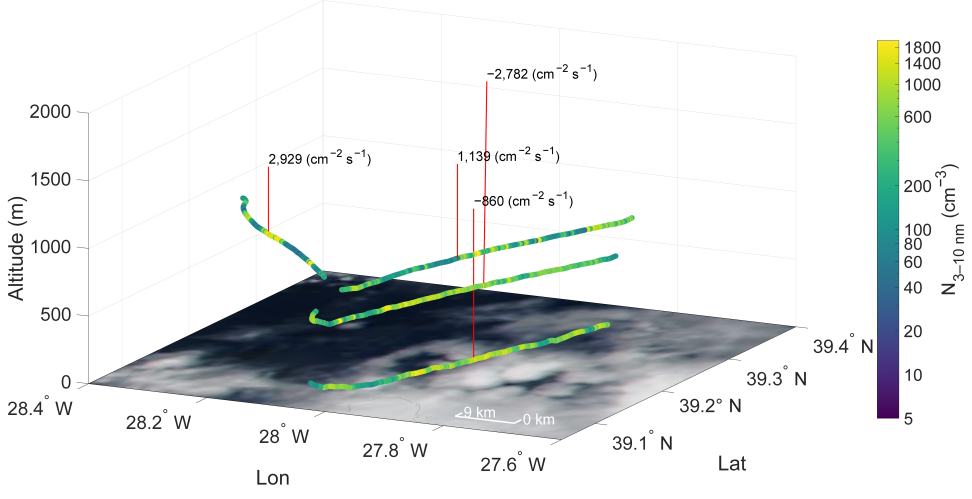

Figure 8. Same as Figure 3, but for June 21, 2017. The background shows a satellite-corrected reflectance image taken from the overpass at 14:15 UTC with the ocean surface appearing dark and clouds appearing white, Credit: NASA Worldview Snapshots.

Figure 8 reveals a strong negative flux of $N_{3–10}$ (−2,782 cm^{-2} s^{-1}) at 550 m that is nearly three times greater in magnitude than the flux at 50 m (−860 cm^{-2} s^{-1}), likely due to particle evolution through growth and coagulation, and dilution processes during vertical transport. The positive fluxes of $N_{3–10}$ observed at 800 m (2,929 and 1,139 cm^{-2} s^{-1}) suggest that nucleation initiated either at the top of the well-mixed boundary layer or at the bottom of the overlying decoupled layer. This bidirectional flux structure suggests that newly formed particles were transported both upward and downward from the formation zone through turbulent mixing. The comprehensive analysis presented in Figs. 6–

https://doi.org/10.5194/egusphere-2026-61
Preprint. Discussion started: 15 January 2026

8, combined with the flux calculations in Table 1, provides some evidence that SPEs can originate within decoupled layer structures, constituting a significant source of secondary marine aerosols in stratified boundary layer conditions.

4. Discussion

This study demonstrates the value of vertical turbulent flux measurements for characterizing new particle formation (NPF) in remote marine boundary layers. By deriving 3–10 nm particle fluxes from aircraft measurements during the ACE-ENA campaign, we identified two mechanistically distinct NPF scenarios that challenge conventional understanding of marine aerosol sources.

Our analysis reveals different NPF mechanisms operating in the marine boundary layer. The first mode – entrainment zone nucleation – occurs at the boundary layer top (1,200–1,400 m) where several factors create favorable conditions: (1) dilution of mixed-layer air by entrained free tropospheric air causes sudden decreases in preexisting aerosol surface area, (2) adiabatic cooling in rising convective plumes reduces saturation vapor pressures, and (3) turbulent fluctuations in temperature and vapor concentration enhance nucleation rates (Größ et al., 2018; Nilsson et al., 2001). Strong downward fluxes (up to −41,092 cm^{-2} s^{-1}) and the absence of 3–10 nm particles above the entrainment zone provide direct evidence that nucleation occurs specifically in this ~200 m layer. The limited horizontal extent (2–9 km) of these events, comparable to the wavelength-to-depth ratios of convective roll vortices (Etling and Brown, 1993; Hartmann et al., 1997), suggests that organized boundary layer convection may concentrate precursor vapors and newly formed particles into coherent structures.

Our analysis reveals a second distinct mode of new particle formation occurring within decoupled marine boundary layer structures, where particles originate at the interface between the well-mixed surface layer and the overlying decoupled layer (~700–800 m altitude). While mechanistically similar to entrainment zone processes through air mass convergence, thermodynamic gradients, and aerosol dilution effects, decoupled layer nucleation occurs within the boundary layer structure rather than at its top, operating under conditions of reduced aerosol surface area concentrations and stratified vertical mixing. This mode exhibits a regional-scale horizontal extent (>50 km) compared to the localized nature (<10 km) of entrainment zone events. The substantial negative flux magnitudes observed at intermediate altitudes (−2,782 cm^{-2} s^{-1} at 550 m) combined with positive fluxes aloft demonstrate active particle redistribution throughout the marine boundary layer, suggesting this mode represents a significant and previously underappreciated source of secondary marine aerosols that can efficiently contribute to regional cloud condensation nuclei budgets through direct incorporation into the surface mixed layer where particles undergo growth to cloud-relevant sizes.

5. Conclusions

The prevailing theoretical framework, based on relatively high sea spray aerosol surface area acting as condensation and coagulation sinks (Bates et al., 1998; Pirjola et al., 2000), predicted that NPF should rarely occur in remote marine boundary layers over open oceans. Our observations demonstrate that this framework is incomplete. Low aerosol

https://doi.org/10.5194/egusphere-2026-61
Preprint. Discussion started: 15 January 2026

surface area and specific meteorological configurations can create localized or regional zones where conditions become favorable. For entrainment zone and decoupled layer events, extremely low aerosol concentrations, combined with turbulent mixing and adiabatic cooling can create a transient "window" where nucleation can proceed despite moderate surface area concentrations lower in the boundary layer. Recent ground-based observations from the same campaign (Zheng et al., 2021) documented frequent NPF events but could not definitively determine vertical location. Our flux-based approach resolves this ambiguity by providing direct evidence of where particles originate relative to the measurement location. The negative (downward) fluxes in Case 1 unambiguously demonstrate an above-aircraft source, while the bidirectional fluxes in Case 2 indicate a distributed source encompassing the measurement altitude. These findings have important implications for understanding marine CCN budgets. Notably, the spatial scales of these two NPF modes differ by an order of magnitude: entrainment zone events exhibited limited horizontal extents (<10 km), consistent with localized convective structures, while decoupled layer events spanned regional scales (50-60 km), suggesting fundamentally different formation mechanisms or persistence of favorable conditions. Entrainment zone nucleation, despite limited horizontal extent, may contribute significantly to CCN populations through sustained downward transport via convective mixing. The calculated flux of −41,092 cm^{-2} s^{-1} integrated over several hours could deliver substantial numbers of particles to the surface mixed layer where they can grow to CCN sizes. Though flux magnitudes for the decoupled layer nucleation events (−2,782 cm^{-2} s^{-1}) are less pronounced, their large spatial extent likely makes even larger contributions to regional CCN budgets.

Climate models have historically followed theoretical expectations that marine boundary layer nucleation should be negligible, instead representing new particles as primarily originating from free tropospheric entrainment or long-range continental transport (Clarke et al., 2013; Logan et al., 2014). Our observations, combined with recent ground-based measurements (Zheng et al., 2021), demonstrate that this representation misses an important aerosol source. The frequent occurrence of NPF events during the ACE-ENA campaign (entrainment zone nucleation in 2 and decoupled layer nucleation in 4 of 39 flights analyzed) suggests that marine boundary layer nucleation – in both modes – may be more climatologically important than previously recognized. Given that marine boundary layer cloud microphysical properties exhibit the highest sensitivity to aerosol changes (Bellouin et al., 2020; Zhang et al., 2024), and that even modest changes in CCN concentrations can substantially affect cloud radiative forcing in these pristine environments, proper representation of NPF sources is critical for reducing uncertainties in aerosol-cloud interaction estimates.

The continuous wavelet transform (CWT) approach proved essential for deriving reliable fluxes from fast-moving aircraft platforms. Traditional eddy covariance methods require stationarity conditions that are difficult to maintain during aircraft sampling, where the platform continuously moves through different air masses. The CWT method's ability to handle non-stationary data while avoiding systematic errors from linear detrending (Rannik and Vesala, 1999; Schaller et al., 2017) enabled flux calculations even during complex meteorological conditions. Our detailed analysis of frequency response and flux loss corrections demonstrates that 1 Hz CPC measurements, while not ideal, can resolve sufficient turbulent scales to capture the dominant flux contributions when proper corrections are applied. As the scientific community works to reduce uncertainties in aerosol-cloud interactions, flux-based approaches offer

https://doi.org/10.5194/egusphere-2026-61
Preprint. Discussion started: 15 January 2026

a promising path forward for understanding how, where, and when new particles form in Earth's remote marine atmosphere.

Several limitations warrant acknowledgment. First, our 3–10 nm size range likely misses the initial nucleation at molecular cluster sizes (~1–3 nm), meaning we observe "small particle events" rather than nucleation itself. However, the rapid appearance of 3–10 nm particles with clear vertical structure in turbulent fluxes provides strong indirect evidence for nearby nucleation. Second, the aircraft's high ground speed (~100 m s^{-1}) compared to typical tower-based measurements introduces challenges for capturing the full turbulent spectrum, particularly at lower altitudes where eddy sizes are smaller. Our flux loss corrections (F_m/F ratios of 0.70–0.99) account for this limitation but introduce additional uncertainty. Third, we cannot determine definitively the exact horizontal extent of NPF events from single aircraft transects, though crosswind sampling provides minimum extent estimates.

Future Directions

This work establishes aircraft-derived aerosol fluxes as a valuable tool for characterizing marine boundary layer aerosol sources. Several directions would advance understanding:

Slower aircrafts: Unmanned aerial vehicles operating at 30–40 m s^{-1} would better resolve small-scale turbulence, particularly near the surface, where flux loss corrections are currently largest, improving flux accuracy and enabling more detailed vertical structure analysis.

Expanded measurements: Simultaneous flux measurements of precursor gases (H_2SO_4, NH_3, amines, organics) would directly test hypotheses about nucleation mechanisms and identify which chemical pathways dominate in different scenarios.

Multi-aircraft coordination: Coordinated measurements from more than one aircraft at different altitudes could directly observe vertical particle transport rates and evolution, constraining growth rates and loss processes during transit.

Longer-term statistics: Expanding beyond campaign-based measurements to seasonal or annual timescales would quantify the climatological importance of different NPF modes and their relationships to synoptic meteorological patterns.

Model evaluation: Using observed fluxes as benchmarks for evaluating marine boundary layer nucleation parameterizations in regional and global models would improve their representation of aerosol-cloud interactions.

Code availability

All the scripts used to make the figures used in this study will be available along with the supplementary information

Data availability

All data from the ACE-ENA campaign are archived at the DOE ARM data center, covering measurements from the ARM Aerial Facility near ARM ENA site on Graciosa Island (June 15, 2017 - February 28, 2018).

https://doi.org/10.5194/egusphere-2026-61
Preprint. Discussion started: 15 January 2026

ARM Aerial Facility (AAF) Merged VAP, https://doi.org/10.5439/1999133, (AAFMERGED, (Mei and Gaustad, 2024)

ARM Aerial Facility (AAF) Merged aerosol size distribution, https://doi.org/10.5439/1905541, (AAFMERGEDAEROSOLSD,(Pekour and Ermold, 2017)

ARM Aerial Facility Isokinetic Inlet, https://doi.org/10.5439/1241544, (AAFINLETISOK, (Koontz et al., 2016)

ARM Aerial Facility (AAF) Aircraft Integrated Meteorological Measurement System (AIMMS) - Meteorological data, https://doi.org/10.5439/1349241, (AAFMETAIMS,(Matthews and Goldberger, 2020)

Interagency Working Group for Airborne Data and Telemetry Systems, https://adc.arm.gov/discovery/#/results/s::aaf%20iwg/iopShortName::aaf2017ace-ena, (IWG ACEENA)

Proton Transfer Reaction Mass Spectrometer (PTR-MS), https://adc.arm.gov/discovery/#/results/instrument_code::ptrms/iopShortName::aaf2017ace-ena, (ACE ENA IOP1 G1 PTRMS)

Author contribution

ARS, MDP, and NM conceptualized the study. ARS performed the data curation, formal analysis, and designed the figures with contributions from MDP and NM. NM acquired the financial support for the project. ARS and NM wrote the paper, and all authors provided input on the paper for revision before submission.

Competing interests

Markus Petters is a member of the editorial board of ACP journal.

Acknowledgements

We acknowledge the Atmospheric Radiation Measurement (ARM) Climate Research Facility, a user facility of the United States Department of Energy (US DOE), Office of Science, sponsored by the Office of Biological and Environmental Research. We thank Dr. Jian Wang and all the staff responsible for the operation of the ACE-ENA campaign. We acknowledge the use of imagery from the NASA Worldview application, part of the NASA Earth Observing System Data and Information System (EOSDIS). AI tools were used to assist with language editing solely for improving phrasing and clarity.

Financial support

This work was supported by the DOE Office of Science, Biological and Environment Research, Grant No. DE-SC0024873

https://doi.org/10.5194/egusphere-2026-61
Preprint. Discussion started: 15 January 2026

References

Andreae, M. O.: Aerosols Before Pollution, Science, 315, 50–51, https://doi.org/10.1126/science.1136529, 2007.

Aubinet, M., Vesala, T., and Papale, D. (Eds.): Eddy Covariance: A Practical Guide to Measurement and Data Analysis, Springer Netherlands, Dordrecht, https://doi.org/10.1007/978-94-007-2351-1, 2012.

Bates, T. S., Kapustin, V. N., Quinn, P. K., Covert, D. S., Coffman, D. J., Mari, C., Durkee, P. A., De Bruyn, W. J., and Saltzman, E. S.: Processes controlling the distribution of aerosol particles in the lower marine boundary layer during the First Aerosol Characterization Experiment (ACE 1), J. Geophys. Res. Atmospheres, 103, 16369–16383, https://doi.org/10.1029/97JD03720, 1998.

Bellouin, N., Quaas, J., Gryspeerdt, E., Kinne, S., Stier, P., Watson-Parris, D., Boucher, O., Carslaw, K. S., Christensen, M., Daniau, A. -L., Dufresne, J. -L., Feingold, G., Fiedler, S., Forster, P., Gettelman, A., Haywood, J. M., Lohmann, U., Malavelle, F., Mauritsen, T., McCoy, D. T., Myhre, G., Mülmenstädt, J., Neubauer, D., Possner, A., Rugenstein, M., Sato, Y., Schulz, M., Schwartz, S. E., Sourdeval, O., Storelvmo, T., Toll, V., Winker, D., and Stevens, B.: Bounding Global Aerosol Radiative Forcing of Climate Change, Rev. Geophys., 58, e2019RG000660, https://doi.org/10.1029/2019RG000660, 2020.

Boers, R. and Eloranta, E. W.: Lidar measurements of the atmospheric entrainment zone and the potential temperature jump across the top of the mixed layer, Bound.-Layer Meteorol., 34, 357–375, https://doi.org/10.1007/BF00120988, 1986.

Carslaw, K. S., Lee, L. A., Reddington, C. L., Pringle, K. J., Rap, A., Forster, P. M., Mann, G. W., Spracklen, D. V., Woodhouse, M. T., Regayre, L. A., and Pierce, J. R.: Large contribution of natural aerosols to uncertainty in indirect forcing, Nature, 503, 67–71, https://doi.org/10.1038/nature12674, 2013.

Clarke, A. D., Freitag, S., Simpson, R. M. C., Hudson, J. G., Howell, S. G., Brekhovskikh, V. L., Campos, T., Kapustin, V. N., and Zhou, J.: Free troposphere as a major source of CCN for the equatorial pacific boundary layer: long-range transport and teleconnections, Atmospheric Chem. Phys., 13, 7511–7529, https://doi.org/10.5194/acp-13-7511-2013, 2013.

Dal Maso, M., Kulmala, M., Riipinen, I., Wagner, R., Hussein, T., Aalto, P. P., and Lehtinen, K.: Formation and growth of fresh atmospheric aerosols: eight years of aerosol size distribution data from SMEAR II, Hyytiälä, Finland, Boreal Environ. Res., 10, 323–336, 2005.

Deardorff, J. W.: Three-dimensional numerical study of turbulence in an entraining mixed layer, Bound.-Layer Meteorol., 7, 199–226, https://doi.org/10.1007/BF00227913, 1974.

Desjardins, R. L., MacPherson, J. I., Schuepp, P. H., and Karanja, F.: An evaluation of aircraft flux measurements of CO2, water vapor and sensible heat, Bound.-Layer Meteorol., 47, 55–69, 1989.

Dewani, N., Sakradzija, M., Schlemmer, L., Leinweber, R., and Schmidli, J.: Dependency of vertical velocity variance on meteorological conditions in the convective boundary layer, Atmospheric Chem. Phys., 23, 4045–4058, https://doi.org/10.5194/acp-23-4045-2023, 2023.

Etling, D. and Brown, R. A.: Roll vortices in the planetary boundary layer: A review, Bound.-Layer Meteorol., 65, 215–248, https://doi.org/10.1007/BF00705527, 1993.

Fan, M. and Pekour, M.: CPC_ACEENA, https://doi.org/10.5439/1440985, 2018.

Foken, T., Wimmer, F., Mauder, M., Thomas, C., and Liebethal, C.: Some aspects of the energy balance closure problem, Atmospheric Chem. Phys., 6, 4395–4402, https://doi.org/10.5194/acp-6-4395-2006, 2006.

https://doi.org/10.5194/egusphere-2026-61
Preprint. Discussion started: 15 January 2026

651 Galewsky, J., Jensen, M. P., and Delp, J.: Marine Boundary Layer Decoupling and the Stable Isotopic Composition
652 of Water Vapor, J. Geophys. Res. Atmospheres, 127, e2021JD035470, https://doi.org/10.1029/2021JD035470, 2022.

653 Gioli, B., Miglietta, F., De Martino, B., Hutjes, R. W. A., Dolman, H. A. J., Lindroth, A., Schumacher, M., Sanz, M.
654 J., Manca, G., Peressotti, A., and Dumas, E. J.: Comparison between tower and aircraft-based eddy covariance fluxes
655 in five European regions, Agric. For. Meteorol., 127, 1–16, https://doi.org/10.1016/j.agrformet.2004.08.004, 2004.

656 Größ, J., Hamed, A., Sonntag, A., Spindler, G., Elina Manninen, H., Nieminen, T., Kulmala, M., Hõrrak, U., Plass-
657 Dülmer, C., Wiedensohler, A., and Birmili, W.: Atmospheric new particle formation at the research station Melpitz,
658 Germany: connection with gaseous precursors and meteorological parameters, Atmospheric Chem. Phys., 18, 1835–
659 1861, https://doi.org/10.5194/acp-18-1835-2018, 2018.

660 Harris, F. J.: On the use of windows for harmonic analysis with the discrete Fourier transform, Proc. IEEE, 66, 51–
661 83, https://doi.org/10.1109/PROC.1978.10837, 1978.

662 Hartmann, J., Kottmeier, C., and Raasch, S.: Roll Vortices and Boundary-Layer Development during a Cold Air
663 Outbreak, Bound.-Layer Meteorol., 84, 45–65, https://doi.org/10.1023/A:1000392931768, 1997.

664 Helbig, M., Gerken, T., Beamesderfer, E. R., Baldocchi, D. D., Banerjee, T., Biraud, S. C., Brown, W. O. J., Brunsell,
665 N. A., Burakowski, E. A., Burns, S. P., Butterworth, B. J., Chan, W. S., Davis, K. J., Desai, A. R., Fuentes, J. D.,
666 Hollinger, D. Y., Kljun, N., Mauder, M., Novick, K. A., Perkins, J. M., Rahn, D. A., Rey-Sanchez, C., Santanello, J.
667 A., Scott, R. L., Seyednasrollah, B., Stoy, P. C., Sullivan, R. C., de Arellano, J. V.-G., Wharton, S., Yi, C., and
668 Richardson, A. D.: Integrating continuous atmospheric boundary layer and tower-based flux measurements to advance
669 understanding of land-atmosphere interactions, Agric. For. Meteorol., 307, 108509,
670 https://doi.org/10.1016/j.agrformet.2021.108509, 2021.

671 Hoose, C., Kristjánsson, J. E., Iversen, T., Kirkevåg, A., Seland, Ø., and Gettelman, A.: Constraining cloud droplet
672 number concentration in GCMs suppresses the aerosol indirect effect, Geophys. Res. Lett., 36, 2009GL038568,
673 https://doi.org/10.1029/2009GL038568, 2009.

674 Horst, T. W.: A Simple Formula for Attenuation of Eddy Fluxes Measured with First-Order Scalar Sensors, Bound.-
675 Layer Meteorol., 82, 219–233, https://doi.org/10.1023/A:1000229130034, 1997.

676 Intergovernmental Panel on Climate Change (IPCC): Climate Change 2021 – The Physical Science Basis: Working
677 Group I Contribution to the Sixth Assessment Report of the Intergovernmental Panel on Climate Change, 1st ed.,
678 Cambridge University Press, https://doi.org/10.1017/9781009157896, 2023.

679 Islam, M. M., Meskhidze, N., Rasheeda Satheesh, A., and Petters, M. D.: Turbulent Flux Measurements of the Near-
680 Surface and Residual-Layer Small Particle Events, J. Geophys. Res. Atmospheres, 127, e2021JD036289,
681 https://doi.org/10.1029/2021JD036289, 2022.

682 Jones, C. R., Bretherton, C. S., and Leon, D.: Coupled vs. decoupled boundary layers in VOCALS-REx, Atmospheric
683 Chem. Phys., 11, 7143–7153, https://doi.org/10.5194/acp-11-7143-2011, 2011.

684 Kaimal, J. C. and Finnigan, J. J.: Atmospheric Boundary Layer Flows: Their Structure and Measurement, Oxford
685 University Press, https://doi.org/10.1093/oso/9780195062397.001.0001, 1994.

686 Koontz, A., Mei, F., and Pekour, M.: aafinletisok.a1, https://doi.org/10.5439/1241544, 2016.

687 Korolev, A. and Isaac, G. A.: Shattering during Sampling by OAPs and HVPS. Part I: Snow Particles, J. Atmospheric
688 Ocean. Technol., 22, 528–542, https://doi.org/10.1175/JTECH1720.1, 2005.

689 Kuang, C. and Mei, F.: Condensation Particle Counter (CPC) Instrument Handbook - Airborne Version,
690 https://doi.org/10.2172/1562676, 2019.

https://doi.org/10.5194/egusphere-2026-61
Preprint. Discussion started: 15 January 2026

691 Kulkarni, P. and Wang, J.: New fast integrated mobility spectrometer for real-time measurement of aerosol size
692 distribution: II. Design, calibration, and performance characterization, J. Aerosol Sci., 37, 1326–1339,
693 https://doi.org/10.1016/j.jaerosci.2006.01.010, 2006a.

694 Kulkarni, P. and Wang, J.: New fast integrated mobility spectrometer for real-time measurement of aerosol size
695 distribution—I: Concept and theory, J. Aerosol Sci., 37, 1303–1325, https://doi.org/10.1016/j.jaerosci.2006.01.005,
696 2006b.

697 Kulmala, M., Petäjä, T., Nieminen, T., Sipilä, M., Manninen, H. E., Lehtipalo, K., Dal Maso, M., Aalto, P. P.,
698 Junninen, H., Paasonen, P., Riipinen, I., Lehtinen, K. E. J., Laaksonen, A., and Kerminen, V.-M.: Measurement of the
699 nucleation of atmospheric aerosol particles, Nat. Protoc., 7, 1651–1667, https://doi.org/10.1038/nprot.2012.091, 2012.

700 Lee, X., Massman, W., and Law, B. (Eds.): Handbook of Micrometeorology: A Guide for Surface Flux Measurement
701 and Analysis, Springer Netherlands, Dordrecht, 250 pp., https://doi.org/10.1007/1-4020-2265-4, 2005.

702 Lenschow, D. H. and Stankov, B. B.: Length Scales in the Convective Boundary Layer, J. Atmospheric Sci., 43, 1198–
703 1209, https://doi.org/10.1175/1520-0469(1986)043<1198:LSITCB>2.0.CO;2, 1986.

704 Li, Y., Wu, Y., Tang, J., Zhu, P., Gao, Z., and Yang, Y.: Quantitative Evaluation of Wavelet Analysis Method for
705 Turbulent Flux Calculation of Non-Stationary Series, Geophys. Res. Lett., 50, e2022GL101591,
706 https://doi.org/10.1029/2022GL101591, 2023.

707 Logan, T., Xi, B., and Dong, X.: Aerosol properties and their influences on marine boundary layer cloud condensation
708 nuclei at the ARM mobile facility over the Azores, J. Geophys. Res. Atmospheres, 119, 4859–4872,
709 https://doi.org/10.1002/2013JD021288, 2014.

710 Martin, S., Beyrich, F., and Bange, J.: Observing Entrainment Processes Using a Small Unmanned Aerial Vehicle: A
711 Feasibility Study, Bound.-Layer Meteorol., 150, 449–467, https://doi.org/10.1007/s10546-013-9880-4, 2014.

712 Mather, J. H. and Voyles, J. W.: The Arm Climate Research Facility: A Review of Structure and Capabilities, Bull.
713 Am. Meteorol. Soc., 94, 377–392, https://doi.org/10.1175/BAMS-D-11-00218.1, 2013.

714 Matthews, A. and Goldberger, L.: Aircraft-Integrated Meteorological Measurement System (AIMMS) Instrument
715 Handbook, https://doi.org/10.2172/1725866, 2020.

716 Mei, F. and Gaustad, K.: ARM Aerial Facility (AAF) Merged Value-Added Product Report for Historical G-1 Field
717 Campaigns, Oak Ridge National Laboratory (ORNL), Oak Ridge, TN (United States). Atmospheric Radiation
718 Measurement (ARM) Data Center, https://doi.org/10.2172/2335708, 2024.

719 Meskhidze, N., Xu, J., Gantt, B., Zhang, Y., Nenes, A., Ghan, S. J., Liu, X., Easter, R., and Zaveri, R.: Global
720 distribution and climate forcing of marine organic aerosol: 1. Model improvements and evaluation, Atmospheric
721 Chem. Phys., 11, 11689–11705, https://doi.org/10.5194/acp-11-11689-2011, 2011.

722 Meskhidze, N., Jaimes-Correa, J. C., Petters, M. D., Royalty, T. M., Phillips, B. N., Zimmerman, A., and Reed, R.:
723 Possible Wintertime Sources of Fine Particles in an Urban Environment, J. Geophys. Res. Atmospheres, 124, 13,055-
724 13,070, https://doi.org/10.1029/2019JD031367, 2019.

725 Misztal, P. K., Karl, T., Weber, R., Jonsson, H. H., Guenther, A. B., and Goldstein, A. H.: Airborne flux measurements
726 of biogenic isoprene over California, Atmospheric Chem. Phys., 14, 10631–10647, https://doi.org/10.5194/acp-14-
727 10631-2014, 2014.

728 Modini, R. L., Ristovski, Z. D., Johnson, G. R., He, C., Surawski, N., Morawska, L., Suni, T., and Kulmala, M.: New
729 particle formation and growth at a remote, sub-tropical coastal location, Atmospheric Chem. Phys., 9, 7607–7621,
730 https://doi.org/10.5194/acp-9-7607-2009, 2009.

https://doi.org/10.5194/egusphere-2026-61
Preprint. Discussion started: 15 January 2026

Nilsson, E. D., Rannik, Ü., Kulmala, M., Buzorius, G., and O'dowd, C. D.: Effects of continental boundary layer evolution, convection, turbulence and entrainment, on aerosol formation, Tellus Ser. B Chem. Phys. Meteorol. B, 53, 441–461, https://doi.org/10.3402/tellusb.v53i4.16617, 2001.

Olfert, J. S., Kulkarni, P., and Wang, J.: Measuring aerosol size distributions with the fast integrated mobility spectrometer, J. Aerosol Sci., 39, 940–956, https://doi.org/10.1016/j.jaerosci.2008.06.005, 2008.

Pekour, M. and Ermold, B.: ARM Aerial Facility (AAF) Merged aerosol size distribution, https://doi.org/10.5439/1905541, 2017.

Petters, M. D., Snider, J. R., Stevens, B., Vali, G., Faloona, I., and Russell, L. M.: Accumulation mode aerosol, pockets of open cells, and particle nucleation in the remote subtropical Pacific marine boundary layer, J. Geophys. Res. Atmospheres, 111, 2004JD005694, https://doi.org/10.1029/2004JD005694, 2006.

Pirjola, L., O'Dowd, C. D., Brooks, I. M., and Kulmala, M.: Can new particle formation occur in the clean marine boundary layer?, J. Geophys. Res. Atmospheres, 105, 26531–26546, https://doi.org/10.1029/2000JD900310, 2000.

Pope, S. B.: Turbulent Flows, 1st ed., Cambridge University Press, https://doi.org/10.1017/CBO9780511840531, 2000.

Pryor, S. C., Larsen, S. E., Sørensen, L. L., Barthelmie, R. J., Grönholm, T., Kulmala, M., Launiainen, S., Rannik, Ü., and Vesala, T.: Particle fluxes over forests: Analyses of flux methods and functional dependencies, J. Geophys. Res., 112, D07205, https://doi.org/10.1029/2006JD008066, 2007.

Quinn, P. K., Coffman, D. J., Johnson, J. E., Upchurch, L. M., and Bates, T. S.: Small fraction of marine cloud condensation nuclei made up of sea spray aerosol, Nat. Geosci., 10, 674–679, https://doi.org/10.1038/ngeo3003, 2017.

Rannik, Ü. and Vesala, T.: Autoregressive filtering versus linear detrending in estimation of fluxes by the eddy covariance method, Bound.-Layer Meteorol., 91, 259–280, https://doi.org/10.1023/A:1001840416858, 1999.

Sakai, R. K., Fitzjarrald, D. R., and Moore, K. E.: Importance of Low-Frequency Contributions to Eddy Fluxes Observed over Rough Surfaces, J. Appl. Meteorol., 40, 2178–2192, https://doi.org/10.1175/1520-0450(2001)040<2178:IOLFCT>2.0.CO;2, 2001.

Schaller, C., Göckede, M., and Foken, T.: Flux calculation of short turbulent events – comparison of three methods, Atmospheric Meas. Tech., 10, 869–880, https://doi.org/10.5194/amt-10-869-2017, 2017.

Schmid, B., Tomlinson, J. M., Hubbe, J. M., Comstock, J. M., Mei, F., Chand, D., Pekour, M. S., Kluzek, C. D., Andrews, E., Biraud, S. C., and McFarquhar, G. M.: The DOE ARM Aerial Facility, Bull. Am. Meteorol. Soc., 95, 723–742, https://doi.org/10.1175/BAMS-D-13-00040.1, 2014.

Schwarz, J. P., Gao, R. S., Fahey, D. W., Thomson, D. S., Watts, L. A., Wilson, J. C., Reeves, J. M., Darbeheshti, M., Baumgardner, D. G., Kok, G. L., Chung, S. H., Schulz, M., Hendricks, J., Lauer, A., Kärcher, B., Slowik, J. G., Rosenlof, K. H., Thompson, T. L., Langford, A. O., Loewenstein, M., and Aikin, K. C.: Single-particle measurements of midlatitude black carbon and light-scattering aerosols from the boundary layer to the lower stratosphere, J. Geophys. Res. Atmospheres, 111, 2006JD007076, https://doi.org/10.1029/2006JD007076, 2006.

Spirig, C., Neftel, A., Ammann, C., Dommen, J., Grabmer, W., Thielmann, A., Schaub, A., Beauchamp, J., Wisthaler, A., and Hansel, A.: Eddy covariance flux measurements of biogenic VOCs during ECHO 2003 using proton transfer reaction mass spectrometry, Atmospheric Chem. Phys., 5, 465–481, https://doi.org/10.5194/acp-5-465-2005, 2005.

Stull, R. B. (Ed.): An Introduction to Boundary Layer Meteorology, Springer Netherlands, Dordrecht, https://doi.org/10.1007/978-94-009-3027-8, 1988.

https://doi.org/10.5194/egusphere-2026-61
Preprint. Discussion started: 15 January 2026

Sun, Y., Jia, L., Chen, Q., and Zheng, C.: Optimizing Window Length for Turbulent Heat Flux Calculations from Airborne Eddy Covariance Measurements under Near Neutral to Unstable Atmospheric Stability Conditions, Remote Sens., 10, 670, https://doi.org/10.3390/rs10050670, 2018.

Torrence, C. and Compo, G. P.: A Practical Guide to Wavelet Analysis., Bull. Am. Meteorol. Soc., 79, 61–78, https://doi.org/10.1175/1520-0477(1998)079<0061:APGTWA>2.0.CO;2, 1998.

Wang, J., Pikridas, M., Spielman, S. R., and Pinterich, T.: A fast integrated mobility spectrometer for rapid measurement of sub-micrometer aerosol size distribution, Part I: Design and model evaluation, J. Aerosol Sci., 108, 44–55, https://doi.org/10.1016/j.jaerosci.2017.02.012, 2017a.

Wang, J., Pikridas, M., Pinterich, T., Spielman, S. R., Tsang, T., McMahon, A., and Smith, S.: A Fast Integrated Mobility Spectrometer for rapid measurement of sub-micrometer aerosol size distribution, Part II: Experimental characterization, J. Aerosol Sci., 113, 119–129, https://doi.org/10.1016/j.jaerosci.2017.05.001, 2017b.

Wang, J., Wood, R., Jensen, M., Azevedo, E., Bretherton, C., and Chand, D.: Aerosol and Cloud Experiments in Eastern North Atlantic (ACE-ENA) Field Campaign Report, 2019.

Weber, R. J., Marti, J. J., McMurry, P. H., Eisele, F. L., Tanner, D. J., and Jefferson, A.: Measurements of new particle formation and ultrafine particle growth rates at a clean continental site, J. Geophys. Res. Atmospheres, 102, 4375–4385, https://doi.org/10.1029/96JD03656, 1997.

Weber, R. J., Clarke, A. D., Litchy, M., Li, J., Kok, G., Schillawski, R. D., and McMurry, P. H.: Spurious aerosol measurements when sampling from aircraft in the vicinity of clouds, J. Geophys. Res. Atmospheres, 103, 28337–28346, https://doi.org/10.1029/98JD02086, 1998.

Wolfe, G. M., Kawa, S. R., Hanisco, T. F., Hannun, R. A., Newman, P. A., Swanson, A., Bailey, S., Barrick, J., Thornhill, K. L., Diskin, G., DiGangi, J., Nowak, J. B., Sorenson, C., Bland, G., Yungel, J. K., and Swenson, C. A.: The NASA Carbon Airborne Flux Experiment (CARAFE): instrumentation and methodology, Atmospheric Meas. Tech., 11, 1757–1776, https://doi.org/10.5194/amt-11-1757-2018, 2018.

Wood, R. and Bretherton, C. S.: Boundary Layer Depth, Entrainment, and Decoupling in the Cloud-Capped Subtropical and Tropical Marine Boundary Layer, J. Clim., 17, 3576–3588, https://doi.org/10.1175/1520-0442(2004)017<3576:BLDEAD>2.0.CO;2, 2004.

Wood, R., Wyant, M., Bretherton, C. S., Rémillard, J., Kollias, P., Fletcher, J., Stemmler, J., de Szoeke, S., Yuter, S., Miller, M., Mechem, D., Tselioudis, G., Chiu, J. C., Mann, J. A. L., O'Connor, E. J., Hogan, R. J., Dong, X., Miller, M., Ghate, V., Jefferson, A., Min, Q., Minnis, P., Palikonda, R., Albrecht, B., Luke, E., Hannay, C., and Lin, Y.: Clouds, Aerosols, and Precipitation in the Marine Boundary Layer: An Arm Mobile Facility Deployment, Bull. Am. Meteorol. Soc., 96, 419–440, https://doi.org/10.1175/BAMS-D-13-00180.1, 2015.

Zhang, J., Chen, Y.-S., Yamaguchi, T., and Feingold, G.: Cloud water adjustments to aerosol perturbations are buffered by solar heating in non-precipitating marine stratocumuli, Atmospheric Chem. Phys., 24, 10425–10440, https://doi.org/10.5194/acp-24-10425-2024, 2024.

Zheng, G., Wang, Y., Aiken, A. C., Gallo, F., Jensen, M. P., Kollias, P., Kuang, C., Luke, E., Springston, S., Uin, J., Wood, R., and Wang, J.: Marine boundary layer aerosol in the eastern North Atlantic: seasonal variations and key controlling processes, Atmospheric Chem. Phys., 18, 17615–17635, https://doi.org/10.5194/acp-18-17615-2018, 2018.

Zheng, G., Wang, Y., Wood, R., Jensen, M. P., Kuang, C., McCoy, I. L., Matthews, A., Mei, F., Tomlinson, J. M., Shilling, J. E., Zawadowicz, M. A., Crosbie, E., Moore, R., Ziemba, L., Andreae, M. O., and Wang, J.: New particle formation in the remote marine boundary layer, Nat. Commun., 12, 527, https://doi.org/10.1038/s41467-020-20773-1, 2021.